Spatial Flux Balance Analysis reveals tissue-of-origin and spatially dependent metabolic rewiring in renal and colorectal cancer

Davide Maspero[1,x], Giovanni Marteletto[2,x], Francesco Lapi[3], Bruno G. Galuzzi[4,5,6], Irene Ruano[1], Ben Vandenbosch[7], Ke Yin[7], Sabine Tejpar[7], Alex Graudenzi[9], Holger Heyn[1,8], Anna Pascual-Reguant[1,+], and Chiara Damiani[3,4,5,+,*]

[1]Centro Nacional de Análisis Genómico, Barcelona, Spain.
[2]Immunobiology Department, Yale School of Medicine, New Haven, USA
[3]Department of Biosciences and Biotecnologies, University of Milano-Bicocca, Milan, Italy
[4]Institute of bioimaging and complex biological systems (IBSBC), Segrate, Italy
[5]SYSBIO Centre of Systems Biology/ ISBE.IT
[6]National Biodiversity Future Center (NBFC)
[7]Department of Oncology, KU Leuven, Leuven, Belgium
[8]Universitat de Barcelona (UB), Barcelona, Spain
[9]Department of Informatics, Systems and Communication, University of Milano-Bicocca, Milan, Italy
[x]These authors contributed equally
[+]Senior authors
[*]Corresponding author

1 Abstract

Spatial metabolomics holds great promise for unraveling the complexities of metabolic reprogramming in cancer, yet its development lags behind the rapid progress of spatial transcriptomics (ST). To bridge this gap and maximize the value of spatial gene expression datasets, we present Spatial Flux Balance Analysis (spFBA), a novel framework that transcends the limitations of existing gene set enrichment methods. The spFBA approach builds upon previous work designed for bulk and single-cell data to return Flux Enrichment Scores, up to the level of single reactions, that can distinguish their preferred directional usage retaining spatial resolution. spFBA integrates differential constraints on flux boundaries in steady-state metabolic modeling, informed by spatial gene expression, and utilizes corner-based flux sampling.

We first tuned and validated spFBA using a publicly available 10x Visium ST dataset from renal cancer samples at the tumor-normal tissue interface. spFBA demonstrated the ability to recapitulate the tissue architecture in renal tumor sections, clearly delineating sustained metabolic growth in the tumor core compared to adjacent normal renal parenchyma. Furthermore, spFBA captured the Warburg effect, revealing distinct metabolic subpopulations within the tumor core, while highlighting lactate excretion as a hallmark across all subpopulations. We then applied spFBA to our own high-resolution ST datasets generated with stereo-seq from a colon cancer patient, including both primary tumor and liver metastases. Unlike the renal case, spFBA uncovered extensive areas of tumor cells consuming lactate in both primary and metastatic sites, with stromal regions in liver metastases producing lactate, suggesting a reverse Warburg effect at play.

These findings highlight that cancer metabolic rewiring and the tumor composition of metabolic subpopulations depend highly on the tissue of origin and the spatial context within the target organ. spFBA emerges as a powerful tool to leverage the rapidly growing collection of spatial gene expression data, offering unprecedented insights into the intricate metabolic landscape of cancer.

2 Introduction

Significant deviations from the typical metabolic programs of normal cells are well-documented in cancer cells. The substantial inter- and intra-tumor heterogeneity observed in these metabolic alterations [1] complicates the identification of specific metabolic pathways for individual tumor types. The inner plasticity of metabolism further exacerbates this challenge. In addition to the well-established adaptability of cell metabolism to nutritional changes, differential wiring of the TCA cycle has been reported between naïve and primed human stem cells [2], highlighting distinct metabolic activity across different mammalian cell states

The metabolic variability across different cell types and cancer clonal populations [3] can be explored through single-cell technologies. However, it is reasonable to expect that the metabolism of a given cell type is influenced by its spatial context, which depends on nutrient diffusion within tissues and varies significantly between tissue types. For instance, the high density of microbial communities in the colon suggests that fermentation byproducts are more likely to be found in the colon than in other tissues [4, 5]. Moreover, this spatial context is shaped by surrounding cells, such as stromal or immune cells, which can interact with cancer cells and contribute to the local availability of metabolites and signaling molecules [6].

We aim to identify and compare spatially related metabolic phenomena across different tumor types, as well as between primary tumors and their metastases. An estimation of the metabolic fluxes with spatial resolution is essential to achieve this goal.

The most direct approach to infer metabolic fluxes is Metabolic Flux Analysis (MFA) [7, 8], which involves iterative fitting of metabolite labeling patterns in isotopic tracers experiments. While spatial metabolomics techniques are developing rapidly, the progress of MFA lags far behind transcriptomics, at the bulk and especially at the single-cell and spatial levels [9, 10, 11]. This gap underscores the need to computationally derive metabolic fluxes from gene expression data. Although various factors, alongside transcriptional regulation, contribute to fluxes and make this task inherently challenging, successful attempts have been made using bulk [12], single-cell [13, 14], or groups of biological samples, such as clusters of single cells identified through cluster analysis [15]. To our knowledge, no attempt has yet been made to model spatial spots or spatial clusters.

Building on prior work using bulk [16] and single-cell RNA-seq data [14, 17], we introduce spatial Flux Balance Analysis (spFBA), a novel framework that processes spatial transcriptomics (ST) data to enrich metabolic fluxes at the spatial spot resolution. spFBA is based on steady-state modeling and integrates the transcriptional information into flux boundary constraints. This approach enables the simulation of fluxes while accounting for indirect transcriptional regulation via substrate availability. spFBA enhances the expressive power of traditional pathway enrichment frameworks used in differential gene expression analysis by capturing differences in reaction directionality and metabolic growth rates. As a result, a detailed and robust enrichment profile of fluxes across any reaction in the metabolic network used as input becomes available for each spatial spot within the ST dataset.

Since we currently lack spatially resolved flux measurements, it is not possible to quantitatively validate spFBA predictions against ground-truth data. Therefore, we validated our approach based on two assumptions: (i) spots with similar gene expression patterns should exhibit similar flux distributions; (ii) cancer tissues should tend to display higher metabolic growth rates than adjacent normal tissues.

To test and apply spFBA, we focused on two tumor types located in tissues with expected heterogeneous nutrient availability: renal cell carcinoma (RCC) and colorectal cancer (CRC). For RCC, we selected a publicly available dataset that includes tumor-tissue interface samples, ideal for testing our computational methodology. For CRC, we generated high-resolution spatial datasets, encompassing both primary and metastatic sites.

We demonstrate the power of scFBA in revealing distinct metabolically-defined subpopulations with spatial arrangements across the analyzed samples. These subpopulations exhibit differential nutrient consumption and secretion patterns, with some consuming and others producing metabolites like lactate.

3 Results

3.1 Spatial Flux Balance Analysis

We developed the spFBA framework, which takes as input any metabolic network model composed of m metabolites and r reactions, either core (e.g., ENGRO2 [16]) or genome-wide (e.g., RECON3D [18]), along with a spatial transcriptomic (ST) dataset containing k spatial spots and n genes. spFBA outputs $k \times r$ Flux Enrichment Scores, providing a score for each reaction in each spatial spot.

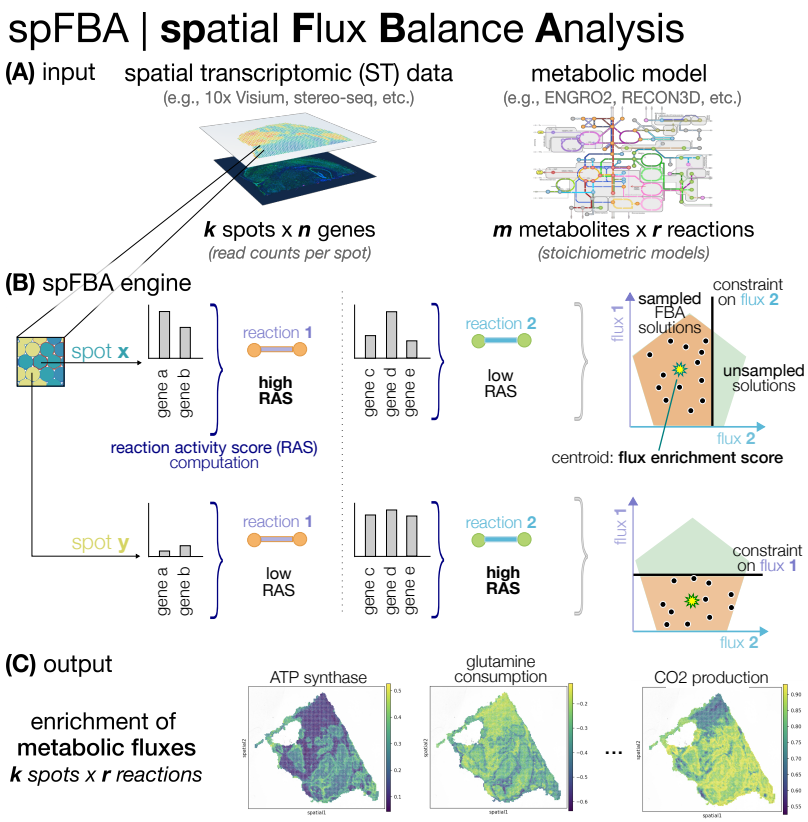

Figure 1: Overview of spFBA. **(A)** spFBA takes two data types as input: 1) a spatial transcriptomic (ST) read counts matrix of a biological sample, in the form of a k spots per n genes matrix; 2) a metabolic network reconstruction, such as ENGRO2 [16], in the form of a m metabolites per r reaction matrix. **(B)** After preprocessing via standard pipelines (see Methods), our framework computes for each reaction in each spot a reaction activity score (RAS), based on the expression level of the genes involved in the reaction. The RAS is then employed to set reaction-specific constraints in the Flux Balance Analysis (FBA) computation. Specifically, a high number of FBA solutions are randomly sampled in the constrained region and, for each reaction, the flux enrichment score is defined as the centroid of the distribution. **(C)** spFBA returns as output the flux enrichment scores, in the form of a k spots per r reactions matrix. Example heatmaps of three reactions are displayed, namely ATP synthase, glutamine consumption, and CO2 production.

To design spFBA, we relied on the constraint-based (CB) modeling framework, which is the most established computational framework for flux simulation [19]. While promising new approaches based on self-supervised learning are emerging, such as scFEA [20], which relax mass balance constraints, they do not provide yet information on critical metabolic outputs, such as growth or energy demands, which are essential for our validation strategy.

Based on our expertise in transcriptionally informed CB methods, we selected the pipe-capacity approach [21] as the foundation for spFBA. We excluded the approach that prunes the reaction network based on transcriptional activity while preserving essential metabolic tasks [22, 23], because setting hard thresholds for gene expression is problematic due to the well-known challenge of defining appropriate cutoffs [24, 25]. Moreover, this binary on-off method may overlook subtler differences in metabolic programs driven by more nuanced variations in gene expression. We also excluded approaches that optimize for expression-like flux distributions [26, 13], where highly expressed reactions carry higher flux, because they assume that more abundant enzymes inherently carry more flux. This assumption, however, disregards enzyme kinetics and the fact that expression levels alone may not always dictate flux capacity.

In our pipe-capacity approach, the entire network topology is retained, but flux boundaries are adjusted based on expression data. While adjusting flux boundaries in a spot-specific manner, we decided to set different flux upper boundaries based on differential expression across spots, rather than within each spot. The assumption that more

abundant enzymes carry more flux is more reasonable when comparing the same enzyme across different spots, where catalytic efficiency is likely conserved. It is worth noting that, since the constraints are defined based on differences across spots, the spot-specific models only become meaningful when analyzed in relation to one another. Therefore, it would be more appropriate to refer to them as spot-relative rather than spot-specific.

Because we want to verify that transcriptionally similar spots have similar flux distributions, spFBA computes a flux enrichment score distribution for each spot independently. Starting from a generic metabolic network model and information about nutrient availability, spFBA first determines, through Flux Variability Analysis (FVA), the region that includes all flux distributions consistent with the steady-state assumption. Spatial transcriptomics data is then used to compute a Reaction Activity Score (RAS) for each reaction in each spot. According to the differences in the RASs across spots, a subregion of the feasible region is determined for each spatial spot independently (spot-relative model).

Once a spot-relative model is obtained, it can be simulated with standard downstream analysis, such as biomass optimization and parsimonious Flux Balance Analysis (pFBA). To release the optimality assumption, spFBA performs flux sampling of the entire feasible region, which, as we will illustrate in the following, proved to be more meaningful.

Finally, spFBA aggregates the sampled fluxes according to their centroids to deliver a final Flux Enrichment Score (FES) for each reaction in each spot.

The overall spFBA framework is schematized in Figure 1.

3.2 spatial FBA well recapitulates the tissue architecture

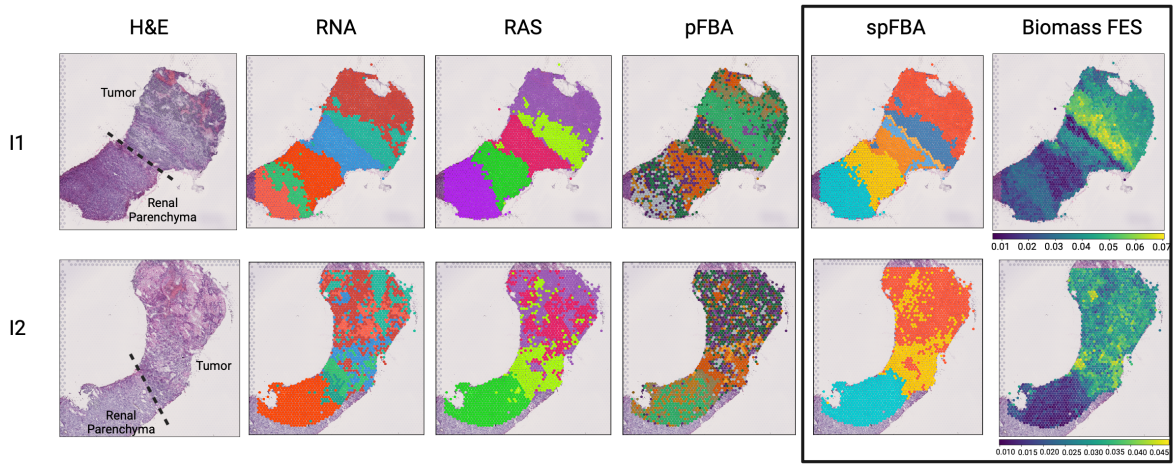

Figure 2: ccRCC samples I1 (top) and I2 (bottom). From left to right: annotated H&E staining taken from [27]; corresponding clustering results obtained with different data layers: RNA (preprocessed reads counts), RAS, pFBA and spFBA. Color scales were independently assigned to clusters, so they are not comparable across layers or samples. Highlighted in the black square, together with the clusters in spFBA layer, are the Biomass FESs obtained with spFBA. The same information for the other ccRCC samples is in supplementary Figures S1 and S2.

As a first validation of the approach, we verified that the enrichment scores (the FESs) produced by scFBA exhibit a coherent spatial distribution. We compared the clustering obtained using different sets of features, representing different biological layers, that is, gene expression, RASs, and fluxes. To make the clustering comparable, we optimized the clustering parameters specifically for each layer. The analysis confirmed that although flux solutions were generated independently for each spot, without considering their spatial coordinates, but only their transcript contents, the clusters obtained using the FES as features exhibit a coherent spatial distribution that well recapitulates the intricate histological architecture displayed in the transcriptomics layer (Fig. 2). This result is not obvious, indeed, as it can be observed in Fig. 2 it does not hold when biomass optimization is performed and the parsimonious optimal flux distribution (obtained with pFBA) is used in place of the normalized sampling centroid. A quantitative comparison of the similarity between clustering results for all ccRCC samples, using the V-measure, is provided in Table S1.

An expected finding, already reported in [14], is that the number of clusters in the fluxomics layer is generally lower than in the counts layer. This indicates that flux distributions can achieve a much lower number of significantly different states, likely because of the lower dimensionality of the fluxome compared to the transcriptome and the lower degrees of freedom for each individual flux, as they are globally constrained by mass balance.

To verify whether metabolic growth rates are higher in the tumor region, we used the flux enrichment score of the biomass pseudo-reaction as a proxy. Figure 2 visualizes the biomass FES in the interface samples I1 and I2, where the authors indicated the division between tumor and healthy tissue [28]. It is possible to observe a clear separation between the two regions, with higher values of biomass enrichment observed in the tumoral region. Although the low resolution hinders accurate pathology annotations, we annotated the other interface samples and observed similar results (Fig. S1).

To highlight the added value of simulation-based enrichment, we qualitatively compared the biomass FES with the information provided by the cell-cycle score, which assigns the most likely phase each cell belongs to based on the expression of predictor genes for each cell-cycle phase [29]. The results reported in Supplementary Fig. S3 indicate that the biomass FES computed by spFBA better distinguishes the tumor core from renal parenchyma.

3.3 Distinct Warburg subpopulations coexist in renal cancer

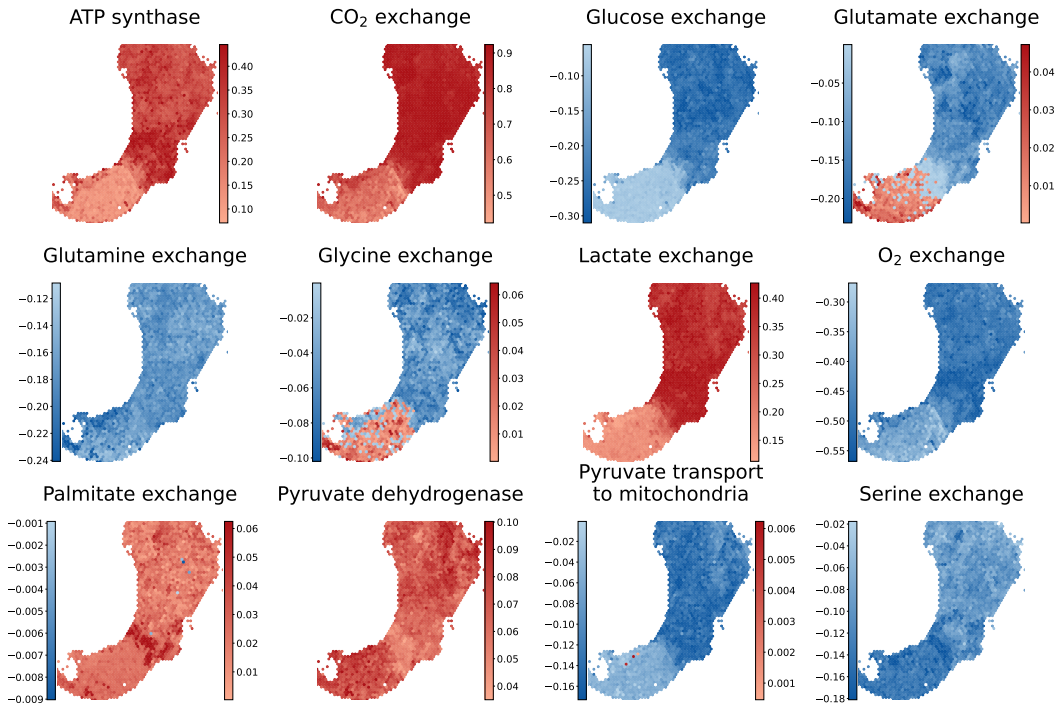

Figure 3: The FES of a set of reactions of interest (in alphabetic order) is visualized for ccRCC sample I2. In the case of exchange reactions, negative values correspond to consumption of the metabolite, positive values to production.

Beyond biomass synthesis, spFBA allows us to analyze the spatial enrichment of any metabolic flux individually. To characterize metabolic reprogramming at spatial resolution, we focused on the metabolic alterations most frequently reported in cancer. A well-known cancer metabolic phenotype is the Warburg Effect, which recently celebrated the 100th anniversary of its first description. Under this effect, cancer cells preferentially generate energy through glycolysis followed by lactic acid fermentation in the cytosol, rather than via the more energy-efficient oxidative phosphorylation in the mitochondria, even when oxygen is largely available [30].

In addition to glucose, other metabolites such as glutamine [31], glutamate [31], serine [32], and glycine [33], have often been correlated with higher proliferation rates. Hence, we also analyzed the consumption/production rates of these amino acids, along with the dynamics of exogenous palmitate, which has been linked with metastasis formation [34].

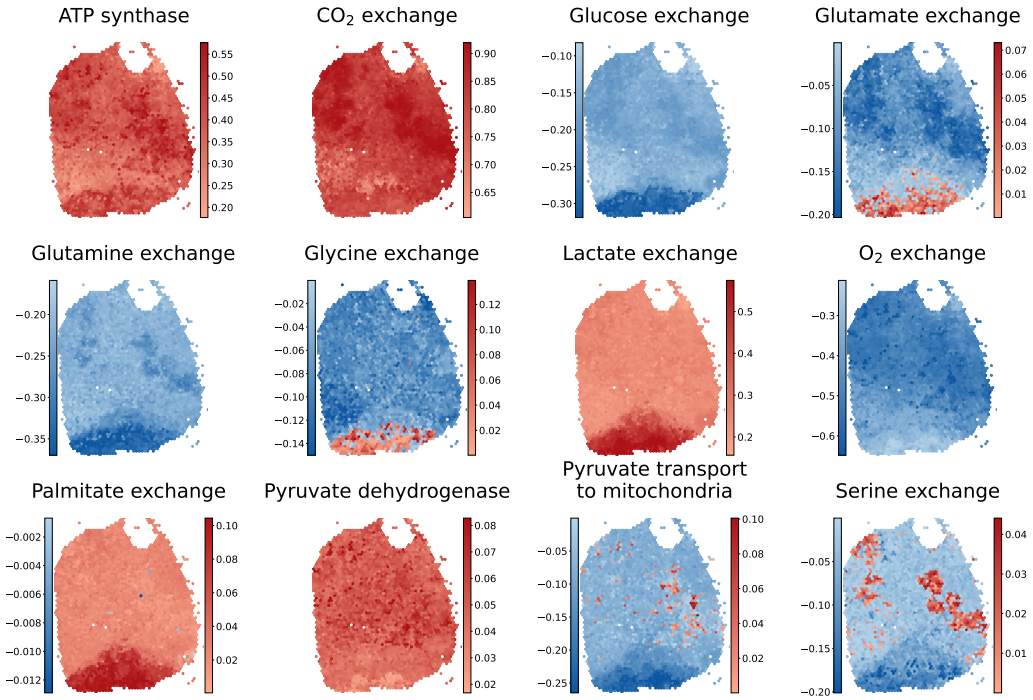

Figure 4: The FES of a set of reactions of interest (in alphabetic order) is visualized for ccRCC sample C1. In the case of exchange reactions, negative values correspond to consumption of the metabolite, positive values to production.

The FESs of the reactions under study are visualized in Fig. 3 for the tumor-normal interface I2, in Figs. S6 to S9 for the other interface samples, and in Figs. 4 and S10 to S13 for the core samples.

When analyzing the tumor-normal interface in Fig. 3, an evident result was that glucose consumption and lactate production are markedly more sustained in the tumor region (corresponding to the upper area, as per annotation in Fig. 2), as expected under the Warburg effect. However, oxygen consumption, CO_2 production, ATP synthesis, in the mitochondria are also enriched in the same region, indicating that cancer cells are generally greedier and metabolically more active. One might be tempted to interpret the production of lactate in this scenario as a simple result of oxygen limitation, where excess glucose that cannot be oxidized is fermented into lactate. However, the situation portrayed by spFBA is far more complex. First, it's important to note that in our simulations, we did not constrain the composition of the medium, which is usually assumed to be nutrient-rich *in vivo* [13]. Instead, we allowed flux sampling of the RAS-informed feasible region to capture different combinations of nutrient intake rates. Therefore, oxygen limitation could potentially emerge from the spRNA-seq data. However, we observed that the flux enrichment score (FES) for pyruvate transport to the mitochondria is negligible in the renal parenchyma and becomes even negative in the tumor area. This indicates that it's not just excess glucose-derived pyruvate failing to be transported into the mitochondria to fuel the TCA cycle and respiratory chain. No glucose-derived pyruvate is oxidized at all. In the tumor region, pyruvate tends to be transported from the mitochondria to the cytosol. It is worth noting that, although the confidence intervals for pyruvate transport (Fig. S4 and S5) confirm shallow usage of the transporter, reverse transport (from mitochondria to cytosol) is less certain, especially in the healthy region.

In [35] it was theoretically shown with a simple metabolic network model that, when available oxygen is not sufficient to fully oxidize all available carbon sources, utilization of glutamine by reductive carboxylation and conversion of glucose and glutamine to lactate confer an advantage for biomass production. A similar situation emerged from the ST data, with the more detailed metabolic network ENGRO2. Higher consumption of the amino acids glutamine, glutamate, and glycine can indeed be observed in the tumor region (Fig. 3).

The situation portrayed by scFBA at the cancer-tissue interface seems more in line with the selfish cell

interpretation of the Warburg effect [36] than with an analogy between Warburg and Crabtree effect [37]. In the latter one would expect a repression of the respiratory chain. However, when we analyzed the tumor core samples, we noticed regions with flux patterns in line with a textbook case of the Crabtree effect. Watching for example sample C1 (Fig. 4) it can be noticed that the bottom region presents a more fermentative behavior, with higher lactate production and glucose intake, but also lower O_2 consumption, as compared to the region above. Remarkably, this bottom fermentation region also displays higher biomass production. All together, these findings highlight a complex landscape of cancer metabolic programs, with coexisting distinct Warburg phenotypes, in ccRCC.

3.4 scFBA can enrich metabolic interactions

A major capability of scFBA as compared to standard enrichment frameworks is the identification of spots with an opposite sign for exogenous nutrients (negative for consumption, positive for production), which is a prerequisite for metabolic cooperation. For example, both in the interface I2 (Fig 3) and in the tumor core C1 (Fig 4) a region can be observed which tends to produce glutamate and glycine, while another region tends to consume them. The former corresponds with the lower oxygen consumption region at the bottom of both samples. Although serine seems to present opposite sign regions in C1 (Figure 4), the positive regions (in red) overlap with large congested blood vessels and multifocal areas of hemorrhage in H&E (Supplementary Figure S2), which might affect the reliability of the results.

It is important to note that we cannot determine whether the populations exchange nutrients among themselves or only with the plasma. Gaining this insight would require experimental measurements of plasma nutrient consumption and secretion rates, which are quite impractical to obtain *in vivo*. Additionally, a population mass balance constraint, as proposed in [14], would be required. Nevertheless, the lack of regions characterized by lactate consumption allows us to rule out the occurrence of metabolic cooperation related to lactate in all ccRCC samples.

Notably, except for a few specific sites that consume exogenous lipids, most tissues rely on de novo lipogenesis to meet the metabolic demands of growth, as it has been reported for many cancer cells [38].

3.5 CRC liver metastasis mimics tissue-of-origin metabolic traits

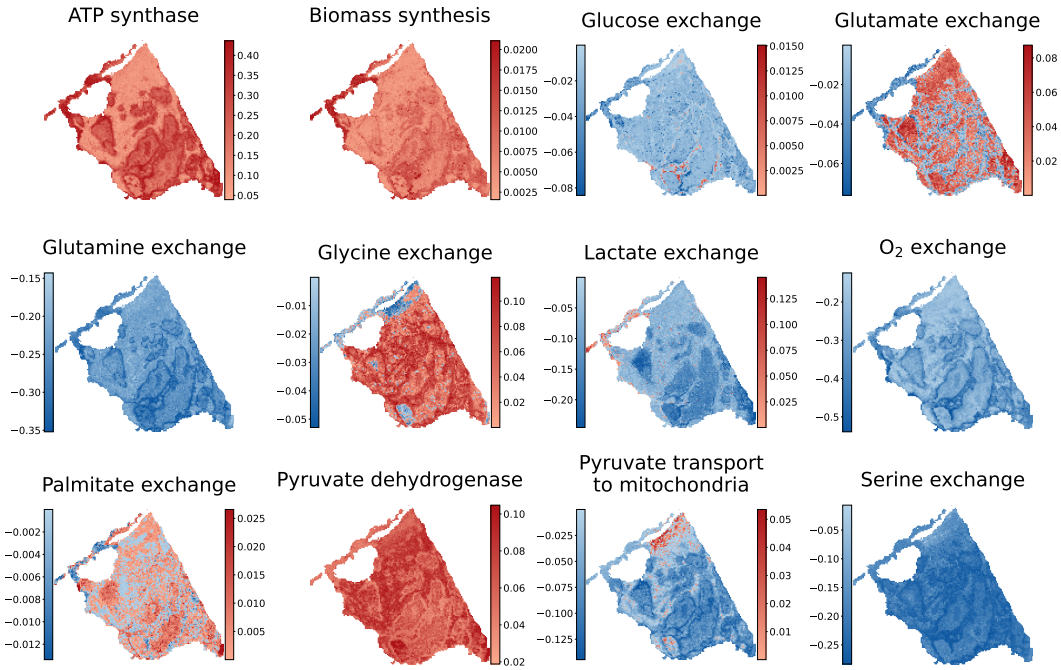

Figure 5: FES of a set of reactions of interest (in alphabetic order) for CRC LM (sample LM4). In the case of exchange reactions, negative values correspond to consumption of the metabolite, positive values to production.

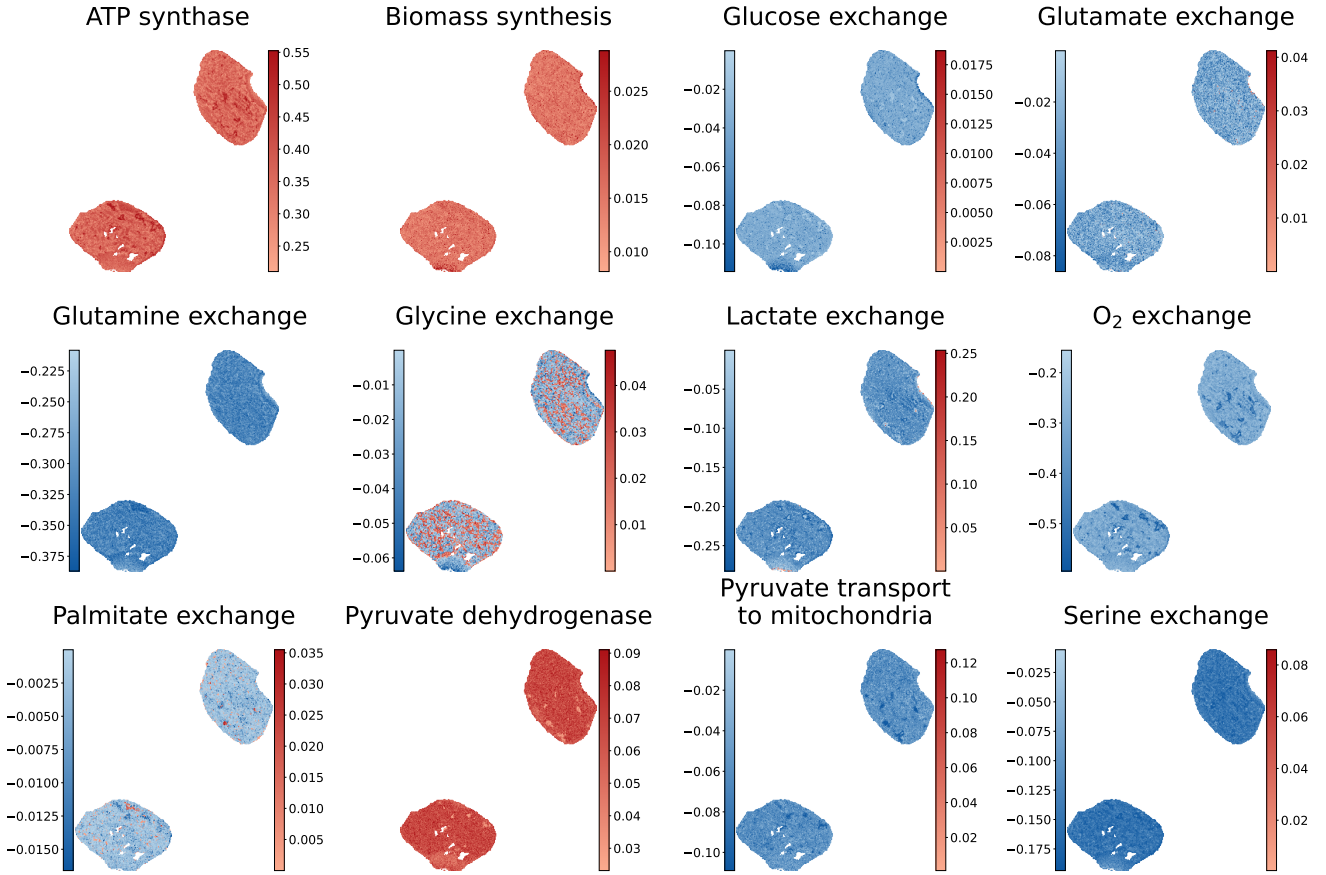

Figure 6: FES of a set of reactions of interest (in alphabetic order) for CRC PT. In the case of exchange reactions, negative values correspond to consumption of the metabolite, positive values to production.

When applying spFBA to our CRC samples, we used the exact same experimental settings as for ccRCC, ensuring that any differences observed in the results are solely due to variations in the spatial transcriptomics (ST) information.

It is particularly striking that, while lactate secretion was consistently detected by spFBA in all ccRCC samples, none of the CRC samples showed any lactate secretion (Fig. 6, S15, 5, and S14). On the contrary, most regions in all CRC samples exhibited an enriched lactate uptake.

We hypothesize that more exogenous lactate is available for both tumor and non-tumor cells to consume in the colon compared to the kidney. This may be due to the presence of various bacteria in the colon capable of producing lactate [39]. In contrast, in the kidney, exogenous lactate is likely less abundant, as supported by literature reporting that kidney cells tend to produce rather than consume lactate [40].

Remarkably, lactate uptake was observed both in the CRC primary tumor (PT) (Fig. 6) and in the liver metastasis (LM) (Fig. S15, 5, S14). The liver is one of the main organs in charge of lactate metabolism, which presents a net uptake of lactate [41]. Therefore, enhanced lactate consumption by metastatic tumor cells might be supported by the pre-existent context of lactate accumulation in physiological conditions. The common utilization of lactate by PT and LM highlighted by scFBA supports the recent hypothesis that differences in tissue nutrient availability might constrain the tissue-of-origin-shaped metabolism of cancer cells to limit sites of metastatic colonization [42]. Metastatic migration of colon cancer cells could be dependent on lactate accessibility of the destination tissue, which enhances the metabolic plasticity of tumor cells to react to changes in nutrient availability, thus maximizing cellular proliferation and growth.

3.6 The reverse Warburg effect takes place in CRC liver metastasis

High-resolution ST allowed us to identify differences in metabolic fluxes between tumor cells and associated stroma. The annotated CRC H&E stained samples are reported in Supplementary Fig. S16. Regarding lactate metabolism, the FES of lactate exchange for the LM in Fig. 5 highlights lighter blue patches that correspond to tumor cells, and darker areas surrounding them that represent the stromal tissue. This contrast indicates that tumor cells present enhanced lactate consumption, whereas some stromal cells seem to be producing lactate Additionally, those stromal regions also showed increased glucose consumption and biomass synthesis. Histologically, stromal regions surrounding the tumor are composed of abundant mature connective tissue with organized cancer-associated fibroblasts (CAFs). Tissue morphology together with spFBA findings support the "reverse Warburg effect" phenomenon, in which CAFs glycolysis metabolically supports adjacent cancer cells [6]. In conclusion, the preexistent context of lactate accumulation exploited by metastatic tumor cells in normal hepatic parenchyma might be further increased by lactate production by CAFs located in the stroma.

It is worth noticing that the reverse Warburg effect is more evident in liver metastases than colon samples, in which not clear areas of tumor associated stroma were annotated and a consequent general lower metabolic heterogeneity was observed (Fig. 6).

Importantly, spFBA is shedding new light on the reverse Warburg effect. In particular, it can be observed that the pyruvate that necessarily derives from lactate consumption is not used to fuel the TCA cycle. On the contrary, pyruvate transport is mainly enriched from mitochondria to cytosol, indicating that lactate-derived pyruvate must be employed in biosynthetic pathways within the cytosol.

3.7 Glutamate exchange and fatty acid biosynthesis are associated with tumor malignancy

As in ccRCC, also in the case of CRC samples, scFBA indicated a possible exchange of glutamate among tumor cell populations. In particular, tumor cells in LM show a preference towards glutamate secretion, whereas stromal cells towards its uptake. On the contrary, tumor cells in PT display a preference for glutamate uptake. According to the literature, glutamate utilization could be related to acquired drug-resistance or epithelial-mesenchymal transition [43].

Worth of note, palmitate accumulation that was uniformly displayed by cancer cells in ccRCC, displays more complex patterns in CRC. While LM tumor cells seem to display a preference towards excess de novo synthesis, surrounding stroma and PT display a preference for utilization of exogenous palmitate.

4 Conclusions

We introduced Spatial Flux Balance Analysis (spFBA), a computational framework to characterize metabolism with spatial resolution by leveraging transcriptomics data.

spFBA demonstrated a unique capability to uncover the spatial metabolic heterogeneity underlying cancer evolution. It confirmed well-established cancer metabolic hallmarks, such as enhanced metabolic growth and the Warburg effect, achieving unprecedented resolution at the level of individual metabolic reactions. This resolution enabled the identification of spatially distinct tumor subpopulations with specific flux distributions.

Unlike standard enrichment approaches that identify active pathways, spFBA provides a deeper insight into the directionality of metabolic fluxes, offering a more nuanced understanding of tumor metabolism. For instance, while enrichment analysis could identify lactate metabolism alterations, spFBA revealed tissue-specific metabolic strategies, such as lactate uptake in colorectal cancer (CRC) compared to secretion in renal cell carcinoma (RCC), indicating distinct metabolic adaptations.

When applied to a new high-resolution colorectal cancer dataset, including primary tumor and matched liver metastasis samples from the same patient, spFBA provided the first clear in vivo evidence of lactate-consuming subpopulations. These findings align with the reverse Warburg effect previously observed in certain cancer cell lines, now revealed with unprecedented spatial detail.

Beyond reproducing known phenomena, spFBA revealed novel metabolic behaviors, such as the decoupling of lactate uptake from oxidative fluxes, opening new avenues for experimental validation and therapeutic intervention. Furthermore, it demonstrated a remarkable similarity between the metabolic behavior of primary CRC tumors and

their metastases, supporting the hypothesis that nutrient availability in the tissue of origin – such as the high levels of lactate in the gut – shapes the metabolic phenotype of metastatic cells.

The ability of spFBA to provide spatially resolved, directional metabolic fluxes makes it a powerful tool not only for studying tumor heterogeneity and progression but also for exploring metabolism across a wide range of tissues and diseases. Importantly, spFBA can be seamlessly applied to the growing wealth of sequencing-based spatial transcriptomics datasets, enabling the fine characterization of metabolic processes without the need for additional experimental data.

5 Methods

5.1 Experimental data

5.1.1 ccRCC dataset

We analyzed a publicly available spatial transcriptomics dataset[44], where kidney samples from 7 patients with Clear Cell Renal Cell Carcinoma (ccRCC) were sequenced using the 10x Visium Genomics protocol.

The patients underwent surgical resection of radiologically diagnosed, treatment-naive renal tumors. Most of the patients were in significantly advanced stages of the disease, we refer the reader to [27] for further details. Among the 16 samples available, we kept 5 samples from the tumor core and 5 from the interface between primary tumor and healthy tissue with higher quality considering metadata annotations provided by the original authors. See table 1.

5.1.2 CRC dataset

We included in this study a primary tumor biopsy (PT) and two liver metastases (*LM4* and *LM7*). Biopsies have been collected in the Department of Oncology University of Leuven from a single patient (*SC087*). For LM4, we generated a technical replicate (*LM4r*). Slices from PT and *LM7* were smaller than LM4, so it was possible to put two consecutive slices on the same stereo-seq chip.

Donors and Sample collection

Biopsies from patients diagnosed with Colorectal Cancer (CRC) and liver metastasis were received fresh after written informed consent, according to the Declaration of Helsinki. Approval by the medical ethics commission of the KU Leuven University (S50887) was obtained, in accordance whith the local ethical guidelines. Samples were collected from a 72 years old male patient. (*SC087*). Before surgery, patient received Cetuximab as a chemoteraphy and Levofolinezuur, Oxaliplatine plus Fluorouracil treatment.

Histological Analysis

To assess the morphological features and tissue structure and preservation, we performed Hematoxylin and Eosin (H&E) staining of each tissue block. The fresh frozen samples were sectioned at a thickness of $10\mu m$ and fixed with methanol. Afterward, sections were incubated with $500\mu l$ of isopropanol for 1 minute. Slides were air-dried for 5-10 minutes, followed by incubation with hematoxylin. Afterward, the slides were washed by immersion in water and air-dried. Subsequently, 1 ml of bluing buffer was applied and washed. Eosin mix was then added to stain the cytoplasmic components and extracellular matrix. After washing, the stained sections were imaged in a microscope using a BF-Epi channel, 4X and 10X objective lenses, with stitching function.

Stereo-seq Tissue Optimization

Tissue optimization was performed using the Stereo-seq Permeabilization kit (Cat. No. 111KP118) and Stereo-seq chip set P (Cat. No. 110CP118) according to the manufacturer's protocol (Stereo-seq permeabilization set user manual, Ver A1) to define the optimal permeabilization time for the tissue samples we specifically wanted to analyze. Briefly, $10\mu m$ tissue sections were prepared from the primary tumor and liver metastasis cryo-blocks and placed on 2 permeabilization slides containing 4 chips each. The tissue layer was thawed to attach it to the surface of the chips. After drying the tissue at $37°C$, the slides were then dipped into pre-chilled 100% methanol at $-20°C$ and incubated for $30°C$ min to fix the tissue. Post fixation, the tissue permeabilization test was performed on these chips by permeabilizing the tissue at 4 different time points (6, 12, 18, and 24 minutes). Afterward, reverse transcription

was carried out at $42°C$ for 1 h in dark, followed by tissue removal at $55°C$ for 1 h. Fluorescence imaging was performed in the TRITC channel with 10X objective, following the imaging guidelines provided by the manufacturer (Guidebook for Image QC & microscope assessment and imaging, Ver A5). The optimal permeabilization time was assessed based on the strongest fluorescence signal with the lowest signal diffusion (crispness of the RNA footprint). We found the optimal permeabilization time for both the primary colon tumor and the liver metastasis to be between 12 and 18 min and, thus, 15 min was used for the spatial transcriptomics assay.

Stereo-Seq Spatial Transcriptomics Assay

The spatial transcriptomics analysis was performed using the Stereo-seq Transcriptomics kit (Cat. No. 111ST114) according to the manufacturer's protocol (Stereo-seq Transcriptomics set user manual, Ver A2). Briefly, cryosectioning, tissue mounting, and fixation were performed exactly as previously described in the protocol for the tissue optimization. Next, each fixed tissue section was stained with Qbit ssDNA reagent. Fluorescence imaging of the single-stranded DNA staining was performed in the FITC channel with a 10X objective, following the imaging guidelines provided by the manufacturer (Guidebook for Image QC & microscope assessment and imaging, Ver A5). Prior to permeabilization, the ssDNA-stained image was also subjected to QC analysis using the imageQC software as recommended by the manufacturer. Tissues were then permeabilized for 15 minutes, as estimated in the tissue permeabilization test.

After washing the chip, reverse transcription was performed at 42 for 3 h. The tissue was then digested and removed from the chip and cDNA was released, collected, and purified following the manufacturer's recommendation. After quality assessment using a bioanalyzer (Agilent), sequencing library preparation was performed using transposase assisted tagmentation reaction. Indexed PCR and library purification were performed to prepare the final sequencing library as per manufacturer's recommendations. Final Stereo-seq libraries were sequenced on MGI/BGI sequencing platforms (DNBSEQTM T7) at the MGI Latvia sequencing facility.

Stereo-Seq Sequencing Processing

We processed each FASTQ file obtained from each sample using the SAW pipeline v.7.1.1 [45]. The pipeline consists of two main steps, which were performed for each sample as follows: 1) *Alignment and Counting*: We used Homo_sapiens.GRCh38.dna.primary_assembly.fa, Ensembl release 111, as the reference genome and the corresponding GTF annotation file (Homo_sapiens.GRCh38.111.gtf). The sample-related chip mask file, which includes the spatial coordinates, was part of the transcriptomic kit provided by STOmics. We reported the sample IDs in Table 1. 2) *Image Registration*: The fluorescence image taken during the *Stereo-Seq Spatial Transcriptomics Assay* was aligned to the count matrix to define the tissue area, filtering out DNA nano-balls that were not under the tissue from the count matrix.

The pipeline outputs the registered image and a table (.gem/.gef) that includes, for each unique combination of gene ID and spatial coordinates (x, y), the number of molecular identifier (MID) counts. This table was further processed with Stereopy v1.3.0 [46] to define the final count matrix by aggregating spatial coordinates into spots of 50×50 DNA nano-balls. Therefore, the dimension of each spot is $25 \times 25\mu m^2$. The obtained count matrix (spot×gene) is stored in a Scanpy object for downstream analyses.

5.2 ST read counts preprocessing

We applied the same preprocessing steps for both Visium and Stereo-seq datasets using Scanpy v1.9.6 [47]. In particular, the expression profile in each spot was normalized by library size (*pp.normalize_total(adata=adata, target_sum=1e4)*) and log-transformed (*pp.log1p(adata)*) as usually done in single-cell data analysis [25].

Subsequently, we ran Principal Component Analysis (*tl.pca(adata, svd_solver='arpack')*) and selected the first 30 PCs as input for k-nearest-neighbor graph (kNN) construction (*pp.neighbors(adata, n_neighbors=10, n_pcs=30)*).

Next, we clustered kNN graph nodes using the Leiden approach (*tl.leiden(adata)*), selecting a resolution specific to each dataset. We explored the data quality by plotting the distribution of detected genes and total counts in each cluster via violin plots. If needed, we removed clusters with particularly low numbers of detected genes and counts. The resulting datasets have the dimensions reported in table 1.

Finally, to reduce data sparsity, we applied MAGIC imputation [48] with default parameters, before processing the datasets with spFBA.

Sample name	Sample ID	Patient ID	Region	Spot area [μm]	Spot #	Unique genes	Mean counts per spot	Mean genes per spot
LM4	A02991A2	SC087	Liver met.	625	9539	24673	3526.04+-1290.24	1630.53+-512.48
LM7	C03445C6	SC087	Liver met.	625	20729	25425	2569.98+-812.26	1348.27+-362.47
PT	C03445G5	SC087	Colon primary tum.	625	14956	25688	5592.64+-2137.28	2224.24+-562.71
LM4r	A03389C5	SC087	Liver met.	625	11919	24974	4912.33+-1389.13	1941.12+-479.57
C1	6800STDY12499410	PD47171	Kidney - Tum. Core	2376	2888	22317	5821.02+-3532.71	2334.16+-1002.04
C5	6800STDY12499413	PD45816	Kidney - Tum. Core	2376	2102	19735	2776.64+-1891.10	1193.50+-549.47
C2	6800STDY12499407	PD43948	Kidney - Tum. Core	2376	832	19822	10290.89+-5756.34	3065.35+-1101.38
C4	6800STDY12499412	PD45814	Kidney - Tum. Core	2376	1026	21488	9650.70+-4667.24	3324.03+-1184.36
C3	6800STDY12499408	PD47512	Kidney - Tum. Core	2376	3800	22184	3323.62+-2214.55	1778.00+-779.10
I4	6800STDY12499502	PD45814	Kidney - Tum. Interface	2376	2657	20693	2215.16+-1544.44	1050.37+-510.51
I2	6800STDY12499506	PD45816	Kidney - Tum. Interface	2376	1777	21399	5384.21+-2836.88	2242.85+-873.76
I5	6800STDY12499508	PD47465	Kidney - Tum. Interface	2376	2609	21840	3565.95+-2075.09	1520.86+-650.56
I3	6800STDY12499406	PD43824	Kidney - Tum. Interface	2376	3153	22149	2479.87+-2041.36	1191.62+-657.54
I1	6800STDY12499411	PD47171	Kidney - Tum. Interface	2376	2048	23116	8371.10+-5489.16	2993.72+-1393.52

Table 1: Dataset metadata. Additional information regarding patient, sample and quality metrics are reported for each dataset.

5.3 Metabolic model

spFBA theoretically accepts any metabolic network model. However, we were more confident using the manually curated, recently published ENGRO2 core network model [16] of the human central carbon and essential amino acids metabolism. ENGRO2 includes 484 reactions, 403 metabolites, and 497 genes, and represents a follow-up of the core model of human central metabolism ENGRO1 [35]. For this model, 337 reactions are associated with a GPR rule. The biomass pseudo-reaction corresponds with the biomass reaction of the Recon3D model, in terms of the set of metabolites considered and corresponding stoichiometric coefficients. We simulated a growth medium condition in which a specific set of metabolites was abundantly available, or open medium. This set included glucose, lactate, oxygen, water, hydrogen, folic acid, and all essential and non-essential amino acids.

5.4 spFBA methodology

5.4.1 Reaction Activity Scores

We computed a Reaction Activity Score (RAS) for each reaction and spot by substituting the mRNA abundances into the corresponding Gene-Protein-Reaction (GPR) rule, as done in [49]. To solve the logical expressions, the minimum transcript value was taken when multiple genes are joined by an AND operator, and the sum of their values was taken when multiple genes are joined by an OR operator. In the case of GPRs combining both operators AND and OR, we respected their standard precedence.

Once a RAS was computed for each reaction in the metabolic model, we obtained a table of dimensions Spots x Reactions, containing the RAS values.

5.4.2 Flux Variability Analysis

To determine the extreme points of the feasible space, that is, the range of possible fluxes that satisfy the mass balance and the medium constraints, we used Flux variability analysis (FVA)[50, 51, 52]. FVA is a constraint-based modeling technique aimed at determining the maximal and minimal possible flux through any reaction of the model. FVA solves the following two linear programming optimization problems (one for minimization and one for maximization) for each flux v_r of interest, with $r = 1, \ldots, R$:

$$\begin{aligned} &\max / \min \ v_j \\ &S \cdot \vec{v} = \vec{0} \\ &\vec{v_L} \leq \vec{v} \leq \vec{v_U} \end{aligned} \tag{1}$$

where S is the stoichiometric matrix provided by a metabolic network model, $\vec{v}$ is the vector representing the flux of each reaction, $\vec{v} = 0$ represents the steady state assumption, and the vectors $\vec{v_L}$ and $\vec{v_U}$ representing the flux boundaries used to mimic as closely as possible the biological process in the analysis and the availability of nutrients

in the medium define the feasible region of steady-state flux distributions.
We assumed a rich open medium where all the metabolites for which an extra-cellular transporter exits are made available in an unlimited quantity, which is 1000 in the default COBRA model.

5.4.3 Spot-relative flux constraints

After the RAS and FVA computation, specific constraints on internal fluxes of the network are built following an approach adapted from [16, 17]. For each reaction $j = 1, \ldots, R$ and spot $s = 1, \ldots, S$, an upper bound U_j^s and a lower bound L_j^s to the flux capacity are defined, based on the following formulas:

$$U_j^s = F_j^u \times \frac{RAS_j^s}{\max_s RAS_j^s}, \tag{2}$$

$$L_j^s = F_j^l \times \frac{RAS_j^s}{\max_c RAS_j^s}, \tag{3}$$

where F_j^u and F_j^l represent the maximum and the minimum flux that reaction j might carry, obtained by FVA, and RAS_j^s is the RAS value for spot s and reaction j. These constraints are used to map the transcriptomics data into spot lattice, with a one-to-one correspondence between the single spot transcriptomics profile and the corresponding network of each spot. Therefore, each sub-network has specific constraints derived from the transcriptomics and defined in Eq. 2 and 3.

5.4.4 Parsimonious FBA

Given the new set of spot-relative constraints for each spot, we used Eq. 1 to determine the flux distribution that optimizes metabolic growth (i.e., the flux of the biomass synthesis pseudo-reaction) for each spot. Because the optimization problem might have alternative solutions, to select a single flux distribution we employed parsimonious FBA (pFBA). pFBA operates in two optimization steps. First, it determines the maximal value of the biomass. Then, it minimizes the total sum of reaction fluxes while maintaining the optimal value of the primary objective [53].

5.4.5 Corner-based sampling

To analyze each spot-relative metabolic network assuming an objective function, spFBA relies on flux sampling of the feasible region to generate a sequence of feasible solutions that satisfy the network constraints. Flux sampling provides information not only on the range of feasible flux solutions, like FVA, but also on their probability.

In this study, we employed an algorithm, called Corner-based Strategy (CBS) [54, 55], to sample the vertices of the feasible region by using different weighted objective functions each time as the objective function. A predefined number of samples is determined. At each iteration, a new objective function is set by randomly assigning weights in the range $[-1, 1]$ and deciding whether the objective function will be maximized or minimized. To account for the different scales of the various reactions in the model, the weights are divided by the FVA maximum value for each specific reaction. Major details of the implementation are reported in Galuzzi et al.[55]. Such an algorithm captures flux distributions qualitatively and quantitatively more heterogeneous compared to classical Hit-and-Run strategies. In this work, we sampled 1000 points for each spot.

5.4.6 Flux Enrichment Score (FES)

For each spot, we calculated a single Flux Enrichment Score (FES) using the following approach. For the pFBA method, we obtained the unique flux distribution by solving the corresponding optimization problem. We then normalized each reaction value by taking the maximum of the FVA if the flux value is positive, and the minimum of the FVA otherwise. This normalization allows us to assign a score between -1 and 1 for each reaction. In the case of the CBS method, we computed the centroid from 1000 samples, which yields a feasible flux distribution based on the average of all sampled fluxes. We then applied the same normalization process as in the pFBA method. For each FES we also computed its 99% confidence interval.

5.4.7 Spots clustering

For each layer of features, namely counts, RAS, and the 2 different types of fluxes (pFBA ad CBS), we first applied Principal Component Analysis (PCA) to reduce the dimensionality of the datasets. The neighborhood graph was computed on the PCA space to create a distance matrix, encoding the connectivity between spots based on Euclidean distance [56]. The Leiden community detection algorithm was then performed to identify the optimal communities representing clusters of well-connected spots within the neighborhood graph [57].

To produce comparable clusters, we optimized the clustering parameters by maximizing the silhouette score [58], by testing different parameter combinations with a grid-search strategy. The parameters optimized included the number of principal components, the number of neighbors when computing the neighborhood graph, and the resolution in the Leiden algorithm.

6 Funding

A.P.R. is supported by grants from the MCIN/AEI/10.13039/501100011033 and FSE+ (RYC2022-035848-I), and from the MICIU/AEI/10.13039/501100011033/ FEDER/UE (PID2023-148687OB-I00). D.M. is supported by the Juan de la Cierva Fellowship (JDC2022-049637-I) from the Spanish Ministry of Science and Innovation (MCIN/AEI/10.13039/501100011033) and the European Union "NextGenerationEU"/PRTR. Stereo-seq data were generated as part of 2023 STOmics Grant 32, offered by BGI Genomics to D.M. C.D. received funding from the European Union – NextGenerationEU within the PRIN 2022 PNRR call (CUP H53D23007680001).

7 Acknowledgments

We sincerely thank Zhigang Lu and his team for preparing and sequencing the CRC samples. We are also deeply grateful to the patients who generously consented to provide tissue samples for this study, making this work possible. We would also like to thank Marco Vanoni for his valuable input during insightful discussions that contributed to this work.

8 Author contributions

Conceptualization, D.M., A.G., H.H, and C.D.; Methodology, G.M., F.L., B.G.G., and C.D.; Software, D.M., G.M., F.L., and B.G.G.; Formal Analysis, D.M., G.M., F.L., B.G.G., and C.D.; Investigation, D.M., G.M., F.L., B.G.G., and I.R.; Resources, B.V., K.Y., and S.T.; Data Curation, D.M., F.L., I.R., and K.Y.; Writing – Original Draft, D.M., G.M., B.G.G., and C.D.; Writing – Review & Editing, D.M., S.T., A.G., H.H., A.P.R., and C.D.; Visualization, D.M., G.M., I.R., and A.G.; Supervision, S.T., H.H., A.P.R., and C.D.; Project Administration, S.T., H.H., and C.D.; Funding Acquisition, D.M., S.T., H.H., and C.D.;

9 Declaration of interests

The authors declare no competing interests.

References

[1] Liu, X. & Locasale, J. W. Metabolomics reveals intratumor heterogeneity–implications for precision medicine. EBioMedicine **19**, 4–5 (2017).

[2] Arnold, P. K. et al. A non-canonical tricarboxylic acid cycle underlies cellular identity. Nature **603**, 477–481 (2022).

[3] Faubert, B., Solmonson, A. & DeBerardinis, R. J. Metabolic reprogramming and cancer progression. Science **368**, eaaw5473 (2020).

[4] Backhed, F., Ley, R. E., Sonnenburg, J. L., Peterson, D. A. & Gordon, J. I. Host-bacterial mutualism in the human intestine. science **307**, 1915–1920 (2005).

[5] Louis, P. & Flint, H. J. Formation of propionate and butyrate by the human colonic microbiota. Environmental microbiology **19**, 29–41 (2017).

[6] Pavlides, S. et al. The reverse warburg effect: aerobic glycolysis in cancer associated fibroblasts and the tumor stroma. Cell cycle **8**, 3984–4001 (2009).

[7] Antoniewicz, M. R. Methods and advances in metabolic flux analysis: a mini-review. Journal of Industrial Microbiology and Biotechnology **42**, 317–325 (2015).

[8] Wiechert, W. 13c metabolic flux analysis. Metabolic engineering **3**, 195–206 (2001).

[9] Santos, A. A. et al. Spatial metabolomics and its application in the liver. Hepatology **79**, 1158–1179 (2024).

[10] Ma, S. et al. High spatial resolution mass spectrometry imaging for spatial metabolomics: Advances, challenges, and future perspectives. TrAC Trends in Analytical Chemistry **159**, 116902 (2023).

[11] Planque, M., Igelmann, S., Campos, A. M. F. & Fendt, S.-M. Spatial metabolomics principles and application to cancer research. Current Opinion in Chemical Biology **76**, 102362 (2023).

[12] Mardinoglu, A., Gatto, F. & Nielsen, J. Genome-scale modeling of human metabolism–a systems biology approach. Biotechnology journal **8**, 985–996 (2013).

[13] Wagner, A. et al. Metabolic modeling of single th17 cells reveals regulators of autoimmunity. Cell **184**, 4168–4185 (2021).

[14] Damiani, C. et al. Integration of single-cell rna-seq data into population models to characterize cancer metabolism. PLoS computational biology **15**, e1006733 (2019).

[15] Gustafsson, J. et al. Generation and analysis of context-specific genome-scale metabolic models derived from single-cell rna-seq data. Proceedings of the National Academy of Sciences **120**, e2217868120 (2023).

[16] Di Filippo, M. et al. Integrate: Model-based multi-omics data integration to characterize multi-level metabolic regulation. PLoS computational biology **18**, e1009337 (2022).

[17] Galuzzi, B. G., Vanoni, M. & Damiani, C. Combining denoising of rna-seq data and flux balance analysis for cluster analysis of single cells. BMC bioinformatics **23**, 445 (2022).

[18] Brunk, E. et al. Recon3d enables a three-dimensional view of gene variation in human metabolism. Nature biotechnology **36**, 272–281 (2018).

[19] Vijayakumar, S., Conway, M., Lió, P. & Angione, C. Seeing the wood for the trees: a forest of methods for optimization and omic-network integration in metabolic modelling. Briefings in bioinformatics **19**, 1218–1235 (2018).

[20] Alghamdi, N. et al. A graph neural network model to estimate cell-wise metabolic flux using single-cell rna-seq data. Genome research **31**, 1867–1884 (2021).

[21] Machado, D. & Herrgård, M. Systematic evaluation of methods for integration of transcriptomic data into constraint-based models of metabolism. PLoS computational biology **10**, e1003580 (2014).

[22] Becker, S. A. & Palsson, B. O. Context-specific metabolic networks are consistent with experiments. PLoS computational biology **4**, e1000082 (2008).

[23] Opdam, S. et al. A systematic evaluation of methods for tailoring genome-scale metabolic models. Cell systems **4**, 318–329 (2017).

[24] Ritchie, M. E. et al. limma powers differential expression analyses for rna-sequencing and microarray studies. Nucleic acids research **43**, e47–e47 (2015).

[25] Heumos, L. et al. Best practices for single-cell analysis across modalities. Nature Reviews Genetics **24**, 550–572 (2023).

[26] Jamialahmadi, O., Hashemi-Najafabadi, S., Motamedian, E., Romeo, S. & Bagheri, F. A benchmark-driven approach to reconstruct metabolic networks for studying cancer metabolism. PLoS computational biology **15**, e1006936 (2019).

[27] Li, R. et al. Mapping single-cell transcriptomes in the intra-tumoral and associated territories of kidney cancer. Cancer Cell **40**, 1583–1599 (2022).

[28] Gerlinger, M. et al. Genomic architecture and evolution of clear cell renal cell carcinomas defined by multiregion sequencing. Nature genetics **46**, 225–233 (2014).

[29] Scialdone, A. et al. Computational assignment of cell-cycle stage from single-cell transcriptome data. Methods **85**, 54–61 (2015).

[30] Warburg, O., Wind, F. & Negelein, E. The metabolism of tumors in the body. The Journal of general physiology **8**, 519 (1927).

[31] Dang, C. V. Glutaminolysis: supplying carbon or nitrogen or both for cancer cells? Cell cycle **9**, 3884–3886 (2010).

[32] Yang, M. & Vousden, K. H. Serine and one-carbon metabolism in cancer. Nature Reviews Cancer **16**, 650–662 (2016).

[33] Jain, M. et al. Metabolite profiling identifies a key role for glycine in rapid cancer cell proliferation. Science **336**, 1040–1044 (2012).

[34] Bergers, G. & Fendt, S.-M. The metabolism of cancer cells during metastasis. Nature Reviews Cancer **21**, 162–180 (2021).

[35] Damiani, C. et al. A metabolic core model elucidates how enhanced utilization of glucose and glutamine, with enhanced glutamine-dependent lactate production, promotes cancer cell growth: The warburq effect. PLoS computational biology **13**, e1005758 (2017).

[36] Liu, Y. & Westerhoff, H. V. 'social'versus 'asocial'cells—dynamic competition flux balance analysis. NPJ systems biology and applications **9**, 53 (2023).

[37] Alberghina, L. The warburg effect explained: integration of enhanced glycolysis with heterogeneous mitochondria to promote cancer cell proliferation. International Journal of Molecular Sciences **24**, 15787 (2023).

[38] Snaebjornsson, M. T., Janaki-Raman, S. & Schulze, A. Greasing the wheels of the cancer machine: the role of lipid metabolism in cancer. Cell metabolism **31**, 62–76 (2020).

[39] Wang, S. et al. Pivotal roles for ph, lactate, and lactate-utilizing bacteria in the stability of a human colonic microbial ecosystem. msystems 5: e00645-20 (2020).

[40] Shimada, S. et al. Metabolic responses of normal rat kidneys to a high salt intake. Function **4**, zqad031 (2023).

[41] Jeppesen, J. B., Mortensen, C., Bendtsen, F. & Møller, S. Lactate metabolism in chronic liver disease. Scandinavian journal of clinical and laboratory investigation **73**, 293–299 (2013).

[42] Sivanand, S. et al. Cancer tissue of origin constrains the growth and metabolism of metastases. Nature Metabolism 1–14 (2024).

[43] Wang, Q. et al. Therapeutic targeting of glutamate dehydrogenase 1 that links metabolic reprogramming and snail-mediated epithelial–mesenchymal transition in drug-resistant lung cancer. Pharmacological Research **185**, 106490 (2022).

[44] Li, R. et al. Mapping single-cell transcriptomes in the intra-tumoral and associated territories of kidney cancer. Cancer Cell **40**, 1583–1599.e10 (2022). URL `https://www.sciencedirect.com/science/article/pii/S1535610822005487`.

[45] SAW: Stereo-seq analysis workflow. https://github.com/STOmics/SAW.

[46] Fang, S. et al. Stereopy: modeling comparative and spatiotemporal cellular heterogeneity via multi-sample spatial transcriptomics. bioRxiv (2023). URL https://www.biorxiv.org/content/early/2023/12/05/2023.12.04.569485.

[47] Wolf, F. A., Angerer, P. & Theis, F. J. Scanpy: large-scale single-cell gene expression data analysis. Genome biology **19**, 1–5 (2018).

[48] Van Dijk, D. et al. Recovering gene interactions from single-cell data using data diffusion. Cell **174**, 716–729 (2018).

[49] Graudenzi, A. et al. Integration of transcriptomic data and metabolic networks in cancer samples reveals highly significant prognostic power. Journal of biomedical informatics **87**, 37–49 (2018).

[50] Mahadevan, R. & Schilling, C. H. The effects of alternate optimal solutions in constraint-based genome-scale metabolic models. Metabolic engineering **5**, 264–276 (2003).

[51] Gudmundsson, S. & Thiele, I. Computationally efficient flux variability analysis. BMC bioinformatics **11**, 1–3 (2010).

[52] Galuzzi, B. G. & Damiani, C. An efficient implementation of flux variability analysis for metabolic networks. In Italian Workshop on Artificial Life and Evolutionary Computation, 58–69 (Springer, 2022).

[53] Lewis, N. E. et al. Omic data from evolved e. coli are consistent with computed optimal growth from genome-scale models. Molecular systems biology **6**, 390 (2010).

[54] Bordel, S., Agren, R. & Nielsen, J. Sampling the solution space in genome-scale metabolic networks reveals transcriptional regulation in key enzymes. PLoS computational biology **6**, e1000859 (2010).

[55] Galuzzi, B. G., Milazzo, L. & Damiani, C. Adjusting for false discoveries in constraint-based differential metabolic flux analysis. Journal of Biomedical Informatics **150**, 104597 (2024).

[56] Becht, E. et al. Dimensionality reduction for visualizing single-cell data using umap. Nature biotechnology **37**, 38–44 (2019).

[57] Traag, V. A., Waltman, L. & Van Eck, N. J. From louvain to leiden: guaranteeing well-connected communities. Scientific reports **9**, 1–12 (2019).

[58] Rousseeuw, P. J. Silhouettes: a graphical aid to the interpretation and validation of cluster analysis. Journal of computational and applied mathematics **20**, 53–65 (1987).

[59] Rosenberg, A. & Hirschberg, J. V-measure: A conditional entropy-based external cluster evaluation measure. In Proceedings of the 2007 EMNLP-CoNLL conference, 410–420 (2007).